

An Enhanced Isothermal Jeans Approach to Constraining Dark Matter Self-Interactions from Galactic Kinematics

Zixiang Jia^{1,2}, Fangzhou Jiang^{2*}, Shubo Li^{3,4,5}, Ran Li^{3,5}, Jing Wang², and Ling Zhu⁶

¹Department of Astronomy, Peking University, Beijing 100871, China

²Kavli Institute for Astronomy and Astrophysics, Peking University, Beijing 100871, China

³School of Physics and Astronomy, Beijing Normal University, Beijing 100875, China

⁴National Astronomical Observatories, Chinese Academy of Sciences, 20A Datun Road, Chaoyang District, Beijing 100101, China

⁵School of Astronomy and Space Science, University of Chinese Academy of Sciences, Beijing 100049, China

⁶Shanghai Astronomical Observatory, Chinese Academy of Sciences, Nandan road 80, Shanghai, 200030, China

arXiv:2601.17118v1 [astro-ph.GA] 23 Jan 2026

Accepted XXX. Received YYY; in original form ZZZ

ABSTRACT

We present an improved semi-analytical model to predict density profiles of self-interacting dark matter (SIDM) halos and apply it to constrain the self-scattering cross section using SPARC galaxy rotation curves. Building on the isothermal Jeans approach, our model incorporates (i) velocity-dependent cross sections, (ii) an empirical treatment of core collapse, and (iii) enhanced robustness for identifying solutions. These advances allow us to fit a large sample of galaxies, including systems with baryon-dominated centers often excluded in earlier studies. We find that roughly 1/6 of galaxies admit both a core-growth and a core-collapse solution, while the rest favor a unique evolutionary state. Joint constraints across the sample reveal clear velocity dependence: the allowed parameter space forms an L-shaped degeneracy, where both nearly constant, low cross sections ($\sigma_0 \sim 2 \text{ cm}^2/\text{g}$, $\omega \gtrsim 500 \text{ km/s}$) and strongly velocity-dependent models ($\sigma_0 \sim 100 \text{ cm}^2/\text{g}$, $\omega \sim 60 \text{ km/s}$) are viable. Adopting the core-growth interpretation yields best-fit values $\sigma_0 \simeq 5 \text{ cm}^2/\text{g}$ and $\omega \simeq 250 \text{ km/s}$. Our constraints are remarkably consistent with previous results derived from a variety of independent probes. Compared to cold dark matter (CDM) models, SIDM outperforms simple adiabatic-contraction profiles and rivals empirical feedback-based CDM profiles, yet shows no correlation with stellar-to-halo mass ratio, a proxy for feedback strength, offering a distinct explanation for dwarf galaxy diversity. Moreover, SIDM does not affect galaxy-halo scaling relations significantly and makes concentration systematically lower. Our results highlight SIDM as a compelling framework for small-scale structure, while future low-mass kinematic data will be crucial for breaking degeneracies in velocity-dependent cross-section models.

Key words: cosmology: dark matter – galaxies: haloes – galaxies: kinematics and dynamics

1 INTRODUCTION

The standard Λ CDM cosmological paradigm has been remarkably successful on cosmological large scales but continues to face challenges on subgalactic scales, particularly in explaining the structural diversity of dwarf galaxies (e.g., Weinberg et al. 2015; Bullock & Boylan-Kolchin 2017). Baryonic processes can account for some of these discrepancies (e.g., Sales et al. 2022), yet self-interacting dark matter (SIDM) offers a compelling alternative that naturally alleviates small-scale tensions without requiring finely tuned baryonic feedback (see Tulin & Yu 2018, for a review). In the SIDM framework, dark matter (DM) particles undergo frequent self-scattering in dense environments, driving a two-stage evolutionary process for DM halos. Initially, scattering thermalizes the halo center, creating a constant-density core. Over time, however, the isothermal core collapses as heat flows outward and the central temperature rises—an outcome of the negative heat capacity of self-gravitating systems.

This gravothermal evolution leads to cusp–core diversity depending on halo formation times and evolutionary stage (e.g., Ren et al. 2019; Yang et al. 2023; Nadler et al. 2023).

The pace of this evolution is governed by the DM self-interaction cross section, making it a crucial parameter for testing the SIDM paradigm. Observational constraints are primarily derived from galactic kinematics, especially rotation curves (e.g. Kaplinghat et al. 2016; Kamada et al. 2017; Sagunski et al. 2021; Gilman et al. 2021; Adhikari et al. 2024; Roberts et al. 2024; Kong & Yu 2025). By fitting theoretical mass models to rotation curves, one can simultaneously infer halo mass, structural parameters, and the degenerate combination of halo age and cross section. Such models often rely on computationally expensive full N -body SIDM simulations (e.g. Rocha et al. 2013; Elbert et al. 2015; Robles et al. 2017) or 1D gravothermal fluid simulations (e.g. Balberg et al. 2002; Pollack et al. 2015; Essig et al. 2019; Nishikawa et al. 2020). These methods are usually computationally costly, or relying on simplifying assumptions such as neglecting baryonic effects.

* Corresponding author: fangzhou.jiang@pku.edu.cn

A more efficient alternative is the isothermal Jeans model

(Kaplinghat et al. 2014, 2016). This semi-analytic method modifies a baseline CDM halo by solving the isothermal Jeans–Poisson equation for the inner core and smoothly connecting it to the CDM-like outer halo where scattering is negligible. Despite its simplicity, the model reproduces simulation results with surprising accuracy (Robertson et al. 2020). It can also incorporate baryonic effects by including a baryonic potential (Kaplinghat et al. 2016) and modeling adiabatic contraction (Jiang et al. 2023). However, the method struggles to capture the second phase of SIDM evolution – gravothermal core-collapse – because the definition of the isothermal radius, valid during core growth, breaks down once collapse begins.

Recent work has proposed an empirical workaround. Yang et al. (2024) showed that the high-density solution to the isothermal Jeans equations, typically discarded, can approximate the core-collapse stage when mirrored around the point where low- and high-density solutions merge. This approach is computationally lightweight and has been successfully applied to compact systems such as the strong lens SDSSJ0946+1006 (Li et al. 2025).

In this study, we build upon the improved implementations of Jiang et al. (2023) and Yang et al. (2024). Specifically, we (i) incorporate velocity-dependent cross sections following Yang & Yu (2022), (ii) enhance the numerical robustness needed to identify multiple solutions and capture core collapse, and (iii) embed these improvements in a forward-modeling framework to fit SPARC (Spitzer Photometry & Accurate Rotation Curves; Lelli et al. 2016) galaxies. These advances allow us to analyze a substantially larger sample of galaxies, including systems with baryon-dominated centers that were previously excluded.

This paper is organized as follows. Section 2 describes our improvements to the isothermal Jeans model. Section 3 details our fitting methodology. Section 4 presents the inferred constraints on the SIDM cross section. Section 5 examines the scatter in our constraints, compares our results with previous studies, assesses the merits of introducing SIDM relative to CDM models that include baryonic effects, and explores the impact of SIDM mass models on galaxy–halo scaling relations. Section 6 summarizes our findings. Throughout, we adopt a flat cosmology with $h = 0.71$, $\Omega_m = 0.266$, $\Omega_\Lambda = 0.734$, $\Omega_b = 0.0465$, $\sigma_8 = 0.801$, and $n_s = 0.963$ (Komatsu et al. 2011).

2 UPGRADED ISOTHERMAL JEANS MODEL

In this section, we present improvements to the isothermal Jeans model, building on the framework of Jiang et al. (2023). After briefly reviewing the standard formulation (Section 2.1), we introduce modifications to incorporate velocity-dependent cross sections (Section 2.2) and describe our empirical treatment of gravothermal core-collapse (Section 2.3).

2.1 The isothermal Jeans model

Following Kaplinghat et al. (2014, 2016), the SIDM effect is modeled as a modification to a CDM halo, by considering two regimes: an inner part that becomes isothermal because of frequent self-scattering, and an outer part where self-interactions are negligible and the halo remains CDM-like. The transition occurs at a characteristic radius, r_1 , defined such that a typical DM particle undergoes one scattering event over the halo age, t_{age} :

$$\frac{4}{\sqrt{\pi}} \rho_{\text{dm}}(r_1) v(r_1) \sigma_m = \frac{1}{t_{\text{age}}}, \quad (1)$$

where $\rho_{\text{dm}}(r)$ is the DM density profile, $v(r)$ is the 1D velocity dispersion of the halo, and σ_m is the self-interaction cross section per unit mass.

Inside r_1 , the halo is assumed to be isothermal and governed by the spherical Jeans equation,

$$\frac{d(\rho_{\text{dm}} v^2)}{dr} + \frac{2\beta}{r} \rho_{\text{dm}} v^2 = -\rho_{\text{dm}} \frac{d\Phi}{dr}, \quad (2)$$

where Φ is the gravitational potential, β is the velocity anisotropy assumed to be zero, and $v(r) = v_0$ is the constant velocity dispersion in the isothermal region. The resulting density profile is

$$\rho_{\text{dm}}(r) = \rho_{\text{dm}0} \exp \left[-\frac{\Phi(r) - \Phi(0)}{v_0^2} \right], \quad (3)$$

where $\rho_{\text{dm}0}$ is the central DM density. The inner halo profile is then solved together with the Poisson equation,

$$\frac{1}{r^2} \frac{d}{dr} (r^2 \frac{d\Phi}{dr}) = 4\pi G (\rho_{\text{dm}} + \rho_b), \quad (4)$$

where ρ_b is the baryon density distribution, which is regarded as an input quantity inferred from observations.

There are two free parameters in the Jeans–Poisson equations: the central density, $\rho_{\text{dm}0}$, and the central velocity dispersion, v_0 . Each pair uniquely specifies a density profile. These parameters are constrained by treating the outer halo as a boundary condition: beyond r_1 , where scattering is rare, the density profile must asymptotically match that of the target CDM halo. Accordingly, $\rho_{\text{dm}0}$ and v_0 are determined by minimizing the mismatch between the isothermal solution and the CDM profile at r_1 . In practice, this is achieved by minimizing the objective function,

$$\delta^2 = \left[\frac{\rho_{\text{iso}}(r_1) - \rho_{\text{cdm}}(r_1)}{\rho_{\text{cdm}}(r_1)} \right]^2 + \left[\frac{M_{\text{iso}}(r_1) - M_{\text{cdm}}(r_1)}{M_{\text{cdm}}(r_1)} \right]^2, \quad (5)$$

where $M(r)$ is the enclosed mass, and the subscripts ‘iso’ and ‘cdm’ refer to the SIDM isothermal solution and the original CDM profile, respectively.

We refer to this procedure as *stitching* an isothermal SIDM core onto the CDM outskirts. The stitching typically yields two solutions, corresponding to distinct local minima of δ^2 . These solutions share similar v_0 but differ in central density $\rho_{\text{dm}0}$, and are therefore classified as the low-density and high-density branches. Among the two, the low-density solution is generally preferred, as it more closely matches the original CDM profile.

Jiang et al. (2023) improved the workflow by incorporating adiabatic contraction of the target CDM halo. Specifically, they first compute the contracted CDM density profile in response to the baryonic distribution, ρ_b , following the method of Gnedin et al. (2004). The same stitching procedure is then applied to this contracted halo. As in Jiang et al. (2023), we approximate the baryonic distribution with a Hernquist profile,

$$\rho_b(r) = \frac{M_b / 2\pi a^3}{(r/a)(1+r/a)^3}, \quad (6)$$

where M_b is the total baryon mass and a is the scale radius. Unlike Jiang et al. (2023), to expedite the adiabatic contraction calculation, we first compute r_1 using eq. (1) and the initial CDM halo, and then apply the Gnedin et al. calculation to the mass shell enclosed by r_1 to obtain the contracted r_1 radius.

2.2 Velocity-dependent cross section

Previous iterations of the isothermal Jeans method typically assumed constant cross section. To incorporate the well-established velocity

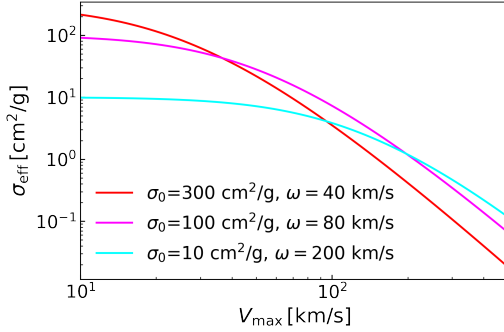


Figure 1. Illustration of effective cross section σ_{eff} as a function of the maximum circular velocity V_{max} of a halo, for velocity-dependent cross section models with different σ_0 and ω , as defined in eq. (7).

dependence, we consider elastic Rutherford scattering between dark matter particles interacting through a Yukawa potential. The corresponding differential cross section in the center-of-momentum frame is

$$\frac{d\sigma}{d\cos\theta} = \frac{\sigma_0 \omega^4}{2[\omega^2 + v^2 \sin^2(\theta/2)]^2}. \quad (7)$$

Following Yang & Yu (2022), we encapsulate this velocity dependence in an effective cross section,

$$\sigma_{\text{eff}} = \frac{1}{2} \int \tilde{v}^2 d\tilde{v} \sin^2 \theta d\cos \theta \frac{d\sigma}{d\cos \theta} \tilde{v}^5 e^{-\tilde{v}^2}, \quad (8)$$

where $\tilde{v} \equiv v/(2v_{\text{eff}})$, and v_{eff} is the characteristic one-dimensional velocity dispersion. For an isotropic velocity field, $v_{\text{eff}} \approx V_{\text{max}}/\sqrt{3}$, where V_{max} is the maximum circular velocity of the input NFW halo. The cross-section model is set by two parameters, σ_0 , the low-velocity normalization, and ω , the velocity scale above which the cross section falls sharply. Fig. 1 illustrates the resulting dependence of σ_{eff} on V_{max} for various (σ_0, ω) . In practice, given a choice of (σ_0, ω) , and a target CDM halo profile, we compute the corresponding σ_{eff} and substitute it for the constant σ_m in the original workflow described in Section 2.1.

2.3 Gravothermal core-collapse

We incorporate an empirical treatment of core-collapse into the isothermal Jeans model by exploiting the behavior of its two solutions. For a fixed cross section, as the halo age t_{age} increases, the central densities $\rho_{\text{dm}0}$ of the low- and high-density solutions gradually converge and eventually merge at a critical time, t_{merge} (see Fig. 2, left). This marks the onset of gravothermal core-collapse, characterized by a subsequent rise in central density. Beyond this point, the standard isothermal Jeans model formally ceases to apply, since the region within r_1 is no longer strictly isothermal.

As a practical workaround, Yang et al. (2024) proposed approximating the post-collapse density profile at $t > t_{\text{merge}}$ using the mirrored high-density solution at $2t_{\text{merge}} - t$. Specifically, they generalize Eq. (1) into:

$$\frac{4}{\sqrt{\pi}} \rho_{\text{dm}}(r_1) v(r_1) \sigma_m = \max \left[\frac{1}{t}, \frac{1}{2t_{\text{merge}} - t} \right]. \quad (9)$$

They demonstrated that this mirrored solution reproduces the core-collapse evolution obtained from gravothermal fluid simulations (e.g., Nishikawa et al. 2020), thus providing a computationally efficient empirical extension of the Jeans model into the collapse regime.

To employ the mirrored high-density solution for describing core-collapse, two requirements must be met: (i) the high-density solution must be identified robustly, and (ii) the merger time, t_{merge} , must be determined accurately. Both tasks are technically challenging because, although the two solutions usually differ by orders of magnitude in central density, they converge rapidly as t_{merge} approaches (see Fig. 2, left). As a result, near $t \sim t_{\text{merge}}$, the search for one solution is inevitably contaminated by the presence of the other. To overcome this difficulty, we refine the stitching procedure. We find that adopting a stringent convergence threshold of $\delta^2 = 10^{-5}$ ensures reliable identification of physically valid solutions. Based on this criterion, we further developed a method to diagnose when a halo has entered the core-collapse phase, along with an efficient algorithm for computing t_{merge} .

In addition, we improve the search algorithm by partitioning the search intervals and exploring the $\rho_{\text{dm}0} - v_0$ space with multiple trials from different initial positions, which improves the recovery of both low- and high-density solutions. Details of these technical improvements are provided in Appendix A. With these upgrades, the isothermal Jeans model can now be applied across all stages of gravothermal evolution. Fig. 2 illustrates the evolution of an SIDM halo with our improved method. We note that halos in the core-growth and core-collapse phases can exhibit nearly identical density profiles when they share the same central density. This degeneracy gives rise to bimodal posteriors encountered in MCMC fits to galaxy rotation curves, as discussed in Section 4.1.

3 FITTING GALAXY ROTATION CURVES

In this section, we describe our procedure for fitting galaxy rotation curves with mass models based on SIDM halos. Section 3.1 introduces the observational sample and selection criteria, Section 3.2 details the modeling of baryonic distributions, and Section 3.3 outlines the fitting strategy.

3.1 Sample selection

We use galaxy rotation curves (RCs) from the public SPARC database (Lelli et al. 2016), which contains 175 late-type galaxies with Spitzer 3.6 μm photometry and high-quality RCs compiled from previous H I/H α observations. The total circular velocity, V_c , is derived from gaseous tracers. Its baryonic contribution consists of a gas component, V_{gas} , obtained from the H I intensity map (with a correction for helium), and a stellar component, V_{\star} , derived from the surface photometry with an assumed mass-to-light ratio. While Lelli et al. (2016) adopt a uniform mass-to-light ratio of unity for all the galaxies, we rescale V_{\star} using a more realistic estimate, as discussed in Section 3.2.

To ensure robust halo mass constraints, we discard galaxies with incomplete RC coverage (fewer than eight data points) or without a clearly defined asymptotically flat region, following Lelli et al. (2016). For some galaxies, their rotation curves marginally pass the selection criteria of Lelli et al. (2016) of showing asymptotically flat region, but the actual data quality is still not good enough for constraining their total masses – manifested by the best-fit virial velocity V_{vir} being higher than the maximum observed rotational velocity V_{max} . We exclude such cases with $V_{\text{vir}}/V_{\text{max}} \geq 1$, where V_{vir} is the virial velocity from the MCMC fitting detailed in Section 3.3. We model the baryonic distribution with a single Hernquist profile, and therefore exclude galaxies showing clear evidence of two stellar components (disk and bulge). We further remove systems whose

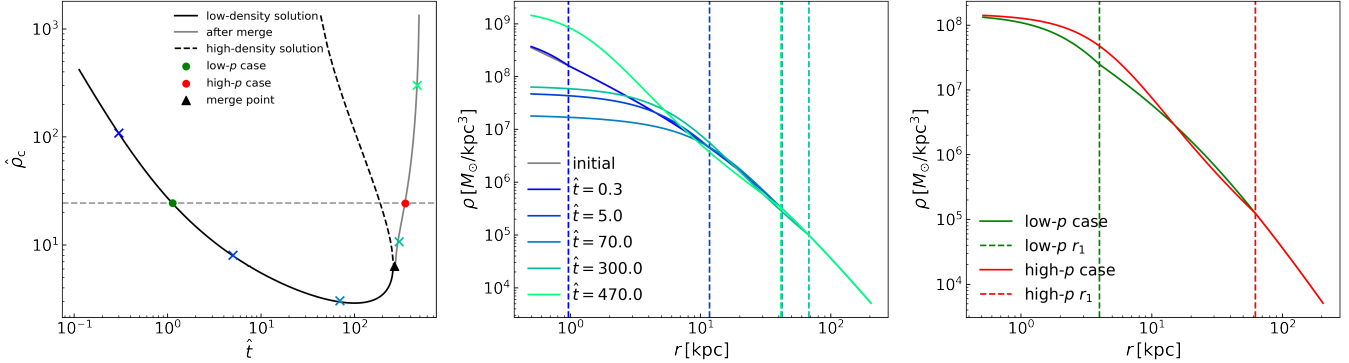


Figure 2. Gravothermal evolution of an SIDM halo modeled with the improved isothermal Jeans method, including an empirical treatment of core-collapse. The example halo has a virial mass of $M_{\text{vir}} = 10^{12} M_{\odot}$, concentration of $c = 10$, and a baryonic component described by a Hernquist profile with a total mass of $M_b = 10^{10} M_{\odot}$ and a scale radius of $a = 5 \text{ kpc}$. *Left:* Evolution of the central density from the low-density (solid black) and high-density (dashed black) solutions. Density and time are shown in dimensionless form $\hat{\rho}_c = \rho_c/\rho_s$, and $\hat{t} = 8\sqrt{G\rho_s}r_s\sigma_{\text{eff}}t_{\text{age}}$, where ρ_s and r_s are the scale density and radius of the target NFW halo. The black triangle marks the merger of the two solutions, indicating the onset of core-collapse. The mirrored high-density branch (grey curve) provides an empirical approximation to the post-collapse evolution, as shown by [Yang et al. \(2024\)](#). Together, the solid curves trace the full gravothermal history. *Middle:* Density profiles along the evolutionary track, marked by crosses in the left panel. As \hat{t} increases, the central density initially decreases as the core expands, reaching its maximum size at $\hat{t} \sim 100$, before shrinking as the central density rises. *Right:* Comparison of core-expanding and core-collapsing halos with identical central density. For example, at $p \equiv \sigma_{\text{eff}}t_{\text{age}} = 1 \text{ cm}^2/\text{g Gyr}$ and $308.5 \text{ cm}^2/\text{g Gyr}$, the central densities coincide and the profiles are similar. This degeneracy underlies the bimodal posteriors found in MCMC fits of SIDM mass models to galaxy rotation curves (see Section 4).

baryonic profiles are poorly fit by a Hernquist model. We end up with 68 galaxies – still among the largest kinematic datasets available for constraining SIDM models.

3.2 Modeling baryon distributions

The efficiency of the isothermal Jeans model relies in part on having an analytical form for the baryonic distribution. We adopt the Hernquist profile as our default description. This choice is motivated both by its wide applicability to dwarf and disc galaxies, and by our use of the [Gnedin et al. \(2004\)](#) method for halo contraction, which assumes a Hernquist baryon distribution for computational efficiency.

The baryonic component includes both gas and stars. The gas mass distribution is directly obtained from $\text{H}\alpha$ observations and is readily available in the SPARC database. For the stellar component, the observed light profile must be converted into a stellar mass profile via the mass-to-light ratio, Γ . However, Γ is uncertain and may vary significantly from one galaxy to another. Since our primary interest lies in dark matter parameters, we determine Γ independently before fitting the rotation curves with SIDM models. We treat Γ as an intrinsic property of the stellar population, independent of the dark matter profile, provided the latter has sufficient flexibility. Thus, by fitting rotation curves with a range of dark matter profiles while allowing Γ to vary freely, the average of the best-fit values offers a reasonable approximation to the intrinsic mass-to-light ratio.

Conveniently, such fits have already been performed: Li et al. (2020) analyzed each SPARC galaxy using multiple dark matter profiles – including NFW (Navarro et al. 1997), coreNFW (Read et al. 2016), DC14 (Di Cintio et al. 2014), Lucky13 (Li et al. 2020), and Einasto (Einasto 1965) – with Γ treated as a free parameter. We adopt their results to compute a weighted average mass-to-light ratio,

$$\Gamma = \frac{\sum \Gamma_i / \sigma_i^2}{\sum 1 / \sigma_i^2}, \quad (10)$$

where the sum is over different profile choices, Γ_i is the best-fit value

for each case, and σ_i is the associated uncertainty. In Appendix B, we show that our mass-to-light ratio is generally consistent with the mean value suggested by stellar population synthesis models.

Finally, we fit a Hernquist circular-velocity profile to the total baryonic rotation curve,

$$V_b^2 = V_{\text{gas}}^2 + V_{\star}^2, \quad (11)$$

We estimate the observed total baryon mass as $M_{b,\text{obs}} = M_\star + M_{\text{gas}}$, where the total stellar mass is $M_\star = \Gamma L_{[3.6]}$, with $L_{[3.6]}$ the total luminosity at 3.6 μm , and the total gas mass is $M_{\text{gas}} = 1.33 M_{\text{HI}}$, with M_{HI} the total H I mass (Lelli et al. 2016). We require the model baryon mass not deviating from $M_{b,\text{obs}}$ by more than 0.5 dex. We restrict our analysis to galaxies whose baryonic distributions are well described by the Hernquist model, excluding the 20% of systems with the largest reduced χ^2 from the Hernquist fits.

3.3 Fitting the SIDM profile

Given the baryonic distribution, an SIDM halo is characterized by three free parameters: virial mass M_{vir} , concentration c , and the product of effective cross section and halo age, $\sigma_{\text{eff}} t_{\text{age}}$, which we denote as p . The likelihood function is defined as

$$\ln \mathcal{P}(\theta | M_{\text{vir}}, c, p) = -\frac{1}{2} \sum_{i=0}^N \left[\frac{V_{c,i} - V_c(R_i | M_{\text{vir}}, c, p)}{\sigma_{V_{c,i}}} \right]^2, \quad (12)$$

where θ represents the observational data: the measured circular velocity $V_{c,i}$ and its uncertainty $\sigma_{V_{c,i}}$ at radius R_i . The model circular velocity is computed as

$$V_c^2 = V_{dm}^2 + V_b^2, \quad (13)$$

where V_b is the observed baryonic contribution given by eq. (11), and V_{dm} is the SIDM halo contribution predicted by the isothermal Jeans model. We set the likelihood function to zero when r_1 is smaller than the radius of the innermost data point in the observed rotation curve.

The posterior distribution of the model parameters, $\mathcal{P}(M_{\text{vir}}, c, p|\theta)$, is given by Bayes' theorem:

$$\mathcal{P}(M_{\text{vir}}, c, p|\theta) \propto \mathcal{P}(\theta|M_{\text{vir}}, c, p)\mathcal{P}(M_{\text{vir}}, c, p), \quad (14)$$

where $\mathcal{P}(M_{\text{vir}}, c, p)$ denotes the prior. We adopt a uniform prior for the logarithmic halo mass

$$\log \frac{M_{\text{vir}}}{M_{\odot}} \in \left[\max \left\{ \log \frac{M_{\text{b}}}{M_{\odot}} + 0.3, 9 \right\}, \min \left\{ \log \frac{M_{\text{b}}}{M_{\odot}} + 4, 13 \right\} \right]. \quad (15)$$

The bounds are motivated by two considerations: (i) virial masses typically exceed baryonic masses by at least 0.3 dex, consistent with the cosmic baryon fraction; and (ii) since SPARC galaxies are predominantly late-type systems, their halos are unlikely to be more massive than those of galaxy groups. For the product of halo age and effective cross section p , we adopt a uniform prior on log scale,

$$\log(p/[\text{cm}^2/\text{g Gyr}]) \in [-2, 4]. \quad (16)$$

The lower bound corresponds to an extremely young halo ($t_{\text{age}} \sim 0.1$ Gyr) with a very small cross section ($0.1 \text{ cm}^2/\text{g}$), while the upper bound corresponds to an old halo with Hubble-time age and a very large cross section ($1000 \text{ cm}^2/\text{g}$). These limits safely encompass all realistic combinations. For halo concentration, we adopt a log-normal prior motivated by the well-established concentration–mass relation, with the median set by a power law and a scatter of 0.11 dex (e.g., [Dutton & Macciò 2014](#)).

We sample the posterior distributions of $\log M_{\text{vir}}$, $\log c$, and $\log p$ using the Markov Chain Monte Carlo (MCMC) method implemented with the ensemble sampler in `emcee` ([Foreman-Mackey et al. 2013](#)). We employ 50 walkers to explore the parameter space with the `StretchMove` algorithm, running each chain for 3000 steps and discarding the first 600 steps as burn-in. To mitigate rare cases where some walkers become trapped in low-posterior regions, we exclude those with anomalously small posterior values.

The determination of t_{merge} during model evaluations is computationally expensive. To accelerate the process, we pre-compute lookup tables of t_{merge} for each galaxy on a grid spanned by $\log(M_{\text{vir}}/M_{\odot})$ and c , given its baryonic distribution.¹ For each model evaluation, t_{merge} is then obtained by cubic-spline interpolation from these pre-computed tables.

The posterior distributions are sometimes bimodal, indicating that either a core-growth or a core-collapse solution can reproduce the data. This is an important aspect of our results and will be discussed further in Section 4.1. To detect and separate bimodal posteriors, we first apply the K-means algorithm in `scikit-learn` ([Pedregosa et al. 2011](#)) to divide the MCMC samples into two clusters. We then assess whether the posterior indeed contains two physically distinct peaks in terms of the parameter p . Specifically, we compute the mean (μ_i) and the standard deviation (σ_i) of $\log p$ within each cluster ($i = 1, 2$), and classify the posterior as bimodal if $|\mu_1 - \mu_2| > 2(\sigma_1 + \sigma_2)$. Visual inspection confirms that this procedure reliably identifies bimodality in p for all applicable galaxies.

4 SIDM MASS MODELS OF SPARC GALAXIES

In this section, we present SIDM mass models for the selected SPARC galaxies, focusing on constraints on the self-interaction cross section, or more precisely, the degenerate product $p \equiv t_{\text{age}}\sigma_{\text{eff}}$. Section 4.1

¹ The grid covers $\max\{\log(M_{\text{b}}/M_{\odot}) + 0.3, 9\} < \log(M_{\text{vir}}/M_{\odot}) < \min\{\log(M_{\text{b}}/M_{\odot}) + 4, 13\}$ and $4 < c < 40$, with 10 evenly spaced points in each dimension.

highlights case studies with unimodal and bimodal posteriors. Section 4.2 then derives effective cross sections σ_{eff} by making physical assumptions on halo age, and performs a joint analysis across the full sample to constrain σ_0 and ω .

4.1 Existence of core-collapsing SIDM halos

Roughly 1/6 of the sample (11 galaxies) exhibits double-peaked posteriors. An example is shown in the upper panels of Fig. 3. This bimodality arises because a halo in the core-growth phase can produce a density profile nearly indistinguishable from that of a core-collapsing halo at later times (see Fig. 2). As a result, both solutions are consistent with the observed rotation curves.

Since p is the product of halo age t_{age} and effective cross section σ_{eff} , a key question for bimodal galaxies is whether the bimodality originates from variations in σ_{eff} or in t_{age} . Clues come from comparing the separation between the p values of the two posteriors with expectations from halo formation-time distributions (see Section 4.2).

Typically, the two p values differ by more than an order of magnitude, while the difference in the two t_{age} values is typically less than an order of magnitude. For example, for a halo of mass $M_{\text{vir}} = 10^{13} M_{\odot}$, the mean lookback time to formation is 6.6 Gyr, while the probability of such a halo forming within the past 1 Gyr is very small, $P(t_{\text{age}} < 1 \text{ Gyr}|M_{\text{vir}}) = 0.0146$. Thus, such large differences in p are unlikely to arise from variations in halo age, and instead imply bimodality in the cross section. For the purpose of constraining cross section, we therefore retain both solutions and explore two scenarios in the following analysis: one in which the low- p solution is adopted, and one in which the high- p solution is taken.

For galaxies with unimodal posteriors, we find that nearly half of them are located near the stage of maximum core size. An example is shown in the lower panels of Fig. 3. The rest of the unimodal sample have only core-growth solutions.

4.2 SIDM cross section

To infer SIDM cross sections from the fitted values of p , we must assume a halo age, t_{age} , for each galaxy. In the absence of direct observational constraints on the assembly histories of SPARC galaxies, we estimate their average formation times as a function of halo mass using extended Press–Schechter theory (e.g., [Lacey & Cole 1993](#)).

For a halo of mass M_0 at redshift z_0 , the probability that it assembled half of its mass by redshift z_1 is

$$\mathcal{P}(>z_1|M_0, z_0) = \int_{M_0/2}^{M_0} \frac{M_0}{M_1} f_{\text{FU}}(S_1, \delta_1|S_0, \delta_0) \left| \frac{dS_1}{dM_1} \right| dM_1, \quad (17)$$

where $S \equiv \sigma^2(M)$ is the variance of the linear density field on mass scale M , and $\delta \equiv 1.686/D(z)$ is the critical linearized overdensity for spherical collapse with $D(z)$ the linear growth rate, and the conditional progenitor mass distribution is

$$f_{\text{FU}}(S_1, \delta_1|S_0, \delta_0) = \frac{1}{\sqrt{2\pi}} \frac{\delta_1 - \delta_0}{(S_1 - S_0)^{3/2}} \exp \left[-\frac{(\delta_1 - \delta_0)^2}{2(S_1 - S_0)} \right]. \quad (18)$$

We adopt the standard halo formation time as the epoch when the halo has assembled half of its present mass, such that \mathcal{P} represents the cumulative probability distribution of formation redshifts. Using the implementation of this formalism in the public code `SatGen`² ([Jiang et al. 2021](#)), we compute the mean formation redshift for halos

² <https://github.com/JiangFangzhou/SatGen>

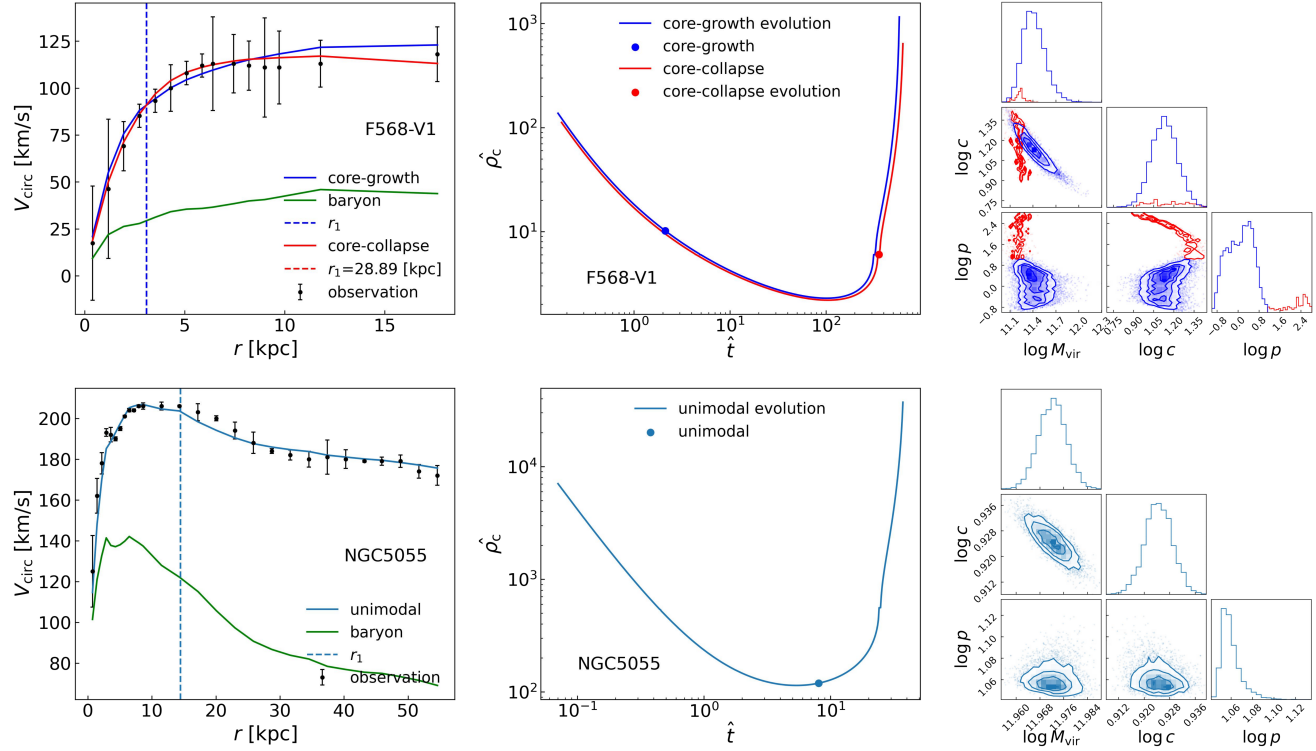


Figure 3. Representative case studies of SIDM rotation-curve fitting. *Left:* Observed circular-velocity profiles (black points with 1σ error bars) from the SPARC survey (Lelli et al. 2016). The baryonic contribution (green curve) is derived from H α intensity and stellar light profiles, with mass-to-light ratios determined as described in Section 3.2. The offset between the data points and the baryonic curve corresponds to the DM contribution. The total mass model, combining the baryonic distribution with the best-fit SIDM halo, is shown by the blue (and red) curves. *Middle:* Evolution of the central density of the best-fit SIDM halos. The filled circles indicate the evolutionary stage that provides the best fit. *Right:* Posterior distributions of the model parameters: halo virial mass M_{vir} , concentration c , and the parameter $p = t_{\text{age}} \sigma_{\text{eff}}$, i.e. the product of halo age and effective cross section. The *upper* row illustrates a case with bimodal posterior: both a core-growth solution ($M_{\text{vir}} = 10^{11.4} M_{\odot}$, $c = 13.5$, and $p = 1.31 \text{ cm}^2 \text{ g}^{-1} \text{ Gyr}$) and a core-collapse solution ($M_{\text{vir}} = 10^{11.2} M_{\odot}$, $c = 14.6$, and $p = 202 \text{ cm}^2 \text{ g}^{-1} \text{ Gyr}$) provide comparably good fits, differing by more than an order of magnitude in p . This bimodality reflects degeneracy in the cross section rather than halo age (see Section 4.1). The *lower* row shows an example with a unimodal posterior: a halo with $M_{\text{vir}} = 10^{12.0} M_{\odot}$, $c = 8.41$, and $p = 11.4 \text{ cm}^2 \text{ g}^{-1} \text{ Gyr}$. This halo lies near the maximal-core stage of gravothermal evolution, as indicated by the circle in the central-density track.

of a given mass, and convert it into the corresponding lookback time, which we take as t_{age} .

For each posterior sample ($\log M_{\text{vir}}$, $\log c$, $\log p$), we compute t_{age} using the method described above and obtain the effective cross section σ_{eff} as $\sigma_{\text{eff}} = p/t_{\text{age}}$. We also calculate the maximum circular velocity V_{max} of the initial NFW halo. By randomly sampling the posterior distributions, we derive the median values and the 68% confidence intervals for both σ_{eff} and V_{max} .

The results are shown in the $\sigma_{\text{eff}} - V_{\text{max}}$ plane in Fig. 4, where several representative velocity-dependent cross-section models (σ_0, ω) are overplotted for comparison. Overall, the galaxies display substantial scatter, with best-fit effective cross sections spanning a wide range. No single cross-section model can account for the full diversity of the sample.

We further constrain the two parameters, σ_0 and ω , in the velocity-dependent cross-section model (eq. (8)), using the inferred values of V_{max} and σ_{eff} for all galaxies. We treat these values as data points, accounting for the uncertainties in σ_{eff} .³ Although no single cross-section model can reproduce all galaxies simultaneously, we can still ask: which models best minimize the overall disagreement? To

quantify this, we define the objective function

$$\chi^2 = \sum_i \left[\frac{\log \sigma_{\text{eff}}(V_{\text{max},i} | \sigma_0, \omega) - \log \sigma_{\text{eff},i}}{\sigma_{\log \sigma_{\text{eff},i}}} \right]^2, \quad (19)$$

where $\sigma_{\text{eff}}(V_{\text{max},i} | \sigma_0, \omega)$ is the model-predicted effective cross section for the i th galaxy given σ_0 and ω , $\sigma_{\text{eff},i}$ is the observationally inferred value, and $\sigma_{\log \sigma_{\text{eff},i}}$ is its uncertainty.

We test whether the population is better explained if bimodal galaxies are all in the core-growth phase vs all in the core-collapse phase. Hence, we derive the constraints on σ_0 and ω under two scenarios for handling these dual-solution systems: (i) adopting only the core-growth solutions, and (ii) adopting only the core-collapse solutions. In either case, these galaxies are analyzed together with those that have a single solution.

The right panels of Fig. 4 show the resulting objective values in the $\sigma_0 - \omega$ plane. More specifically, the plotted quantity is $\Delta \log \chi^2 = \log \chi^2(\omega, \sigma_0) - \log \chi^2_{\text{min}}$, where χ^2_{min} is minimum value across the parameter space, corresponding to the best-fit model. When adopting the core-growth solutions for bimodal systems, we find a clear anti-correlation between σ_{eff} and V_{max} . The resulting joint constraint forms an L-shaped degeneracy in the $\sigma_0 - \omega$ plane. Both strongly velocity-dependent models – with large $\sigma_0 \sim 100 \text{ cm}^2/\text{g}$ and low $\omega \sim 60 \text{ km/s}$ – and nearly constant cross-section models –

³ For simplicity, we neglect the uncertainties in V_{max} .

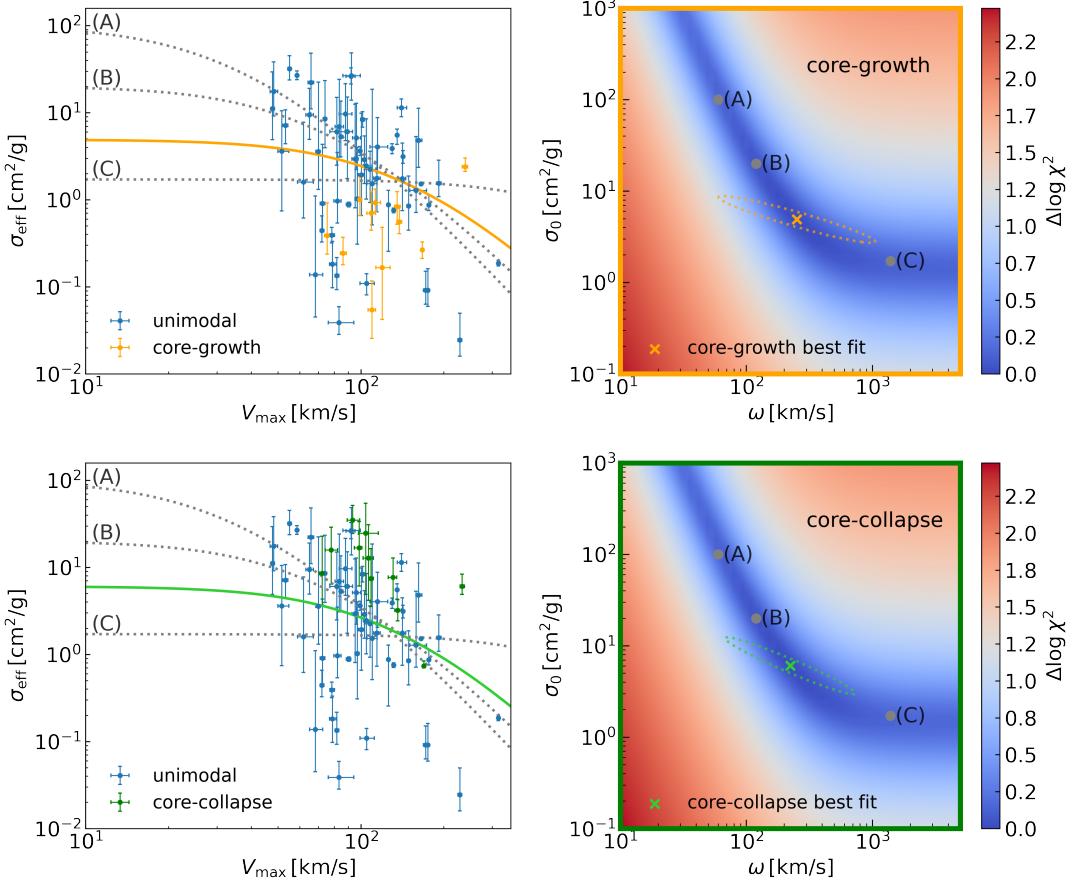


Figure 4. Maximum circular velocities (V_{\max}) and effective cross sections (σ_{eff}) inferred from SIDM mass-model fits to galaxy rotation curves (left), and the resulting joint constraints on the cross-section parameters σ_0 and ω (right). Blue symbols denote galaxies with unimodal posterior. Orange and green symbols represent the core-growth and core-collapse solutions, respectively, for galaxies with bimodal posteriors. Error bars indicate 68% confidence intervals. The joint constraints on σ_0 and ω are obtained by fitting the effective cross section defined in eq. (8) to the (V_{\max} , σ_{eff}) data. In the right panels, we adopt the core-growth and core-collapse solutions, respectively, for bimodal galaxies, while including unimodal galaxies in both analyses. The color scale indicates the χ^2 values relative to the minimum in the σ_0 - ω space (eq. (19)). Constraints on the parameters do not significantly depend on the choice of solutions. With either core-growth or core-collapse solutions, the allowed region forms a clear L-shaped band, where both high- σ_0 low- ω and low- σ_0 high- ω models are comparably viable. Three representative examples (A, B, and C) illustrate this degeneracy. When adopting core-growth solutions, the best-fit MCMC model lies between (B) and (C), with $\sigma_0 = 4.9 \text{ cm}^2/\text{g}$ and $\omega = 250 \text{ km/s}$, marked by an orange cross and a surrounding contour approximating the 3σ posterior interval; the corresponding $\sigma_{\text{eff}}(V_{\max})$ relation is shown by the orange curve. When adopting core-collapse solutions instead, the parameter constraints tighten and the L-shaped allowed region narrows slightly. The best-fit model is similar, given by $\sigma_0 = 6.0 \text{ cm}^2/\text{g}$ and $\omega = 220 \text{ km/s}$, marked by a green cross with a 3σ contour, and its $\sigma_{\text{eff}}(V_{\max})$ relation is shown by the green curve. Without kinematics data for ultra-faint dwarfs ($V_{\max} \lesssim 30 \text{ km/s}$), these degeneracies remain difficult to break.

with $\sigma_0 \sim 2 \text{ cm}^2/\text{g}$ and $\omega \gtrsim 500 \text{ km/s}$ – are comparably favored. The constraints on the parameter space do not exhibit significant dependence on the choice of solutions. When adopting the core-collapse solutions, the constraints on the parameters are slightly strengthened, and the L-shaped allowed region becomes slightly narrower, as shown in the lower right panel of Fig. 4.

Besides scanning the parameter space to evaluate χ^2 , we also infer σ_0 and ω using Bayesian approach with MCMC via the emcee ensemble sampler. The posterior is given by

$$\mathcal{P}(\sigma_0, \omega | \Theta) \propto \mathcal{P}(\Theta | \sigma_0, \omega) \mathcal{P}(\sigma_0, \omega), \quad (20)$$

where Θ denotes the inferred $(V_{\max}, \sigma_{\text{eff}})$ values from the RC fits, $\mathcal{P}(\sigma_0, \omega)$ is the prior, and the likelihood is defined as:

$$\ln \mathcal{P}(\Theta | \sigma_0, \omega) = -\frac{1}{2} \chi^2. \quad (21)$$

We adopt uniform priors of $[-1, 3]$ for $\log(\sigma_0 / [\text{cm}^2/\text{g}])$ and $[1, 3.7]$

for $\log(\omega / [\text{km/s}])$. The posterior is sampled with 50 walkers run for 3000 steps, discarding the first 600 burn-in steps. The resulting posteriors in $(\log \sigma_0, \log \omega)$ are compact and well approximated by two-dimensional Gaussians, shown as 3σ contours in Fig. 4. For the core-growth cases (together with unimodal galaxies), the posterior medians are $\sigma_0 = 4.9 \text{ cm}^2/\text{g}$ and $\omega = 250 \text{ km/s}$. For the core-collapse cases (plus unimodal galaxies), the medians shift to $\sigma_0 = 6.0 \text{ cm}^2/\text{g}$ and $\omega = 220 \text{ km/s}$. The medians do not show a significant difference, which further indicates that the choice of solutions has no substantial impact on the constraints of the parameter space.

We emphasize that no single cross-section model provides a satisfactory fit to all galaxies, and therefore the tight MCMC posteriors should not be over-interpreted. The L-shaped degeneracy seen in the χ^2 maps reinforces this point. The MCMC results primarily serve the purpose of identifying the more probable regions within a degenerate parameter space.

5 DISCUSSION

In this section, we place our results in the context of previous studies and the broader literature on the galaxy–halo connection.

In Section 5.1, we compare our constraints with those obtained in previous studies. In Section 5.2, we investigate the origin of the large scatter in the $\sigma_{\text{eff}}\text{--}V_{\text{max}}$ plane and discuss the prospects and limitations of using individual galaxies to infer the self-interaction cross section.

A common concern regarding the SIDM paradigm is that, by introducing an additional degree of freedom relative to CDM, it may naturally reproduce the observed diversity of galaxy rotation curves. However, within the standard CDM framework, a non-negligible level of structural diversity can also arise once the response of dark-matter halos to baryonic processes is taken into account. Accordingly, in Section 5.3 and Section 5.4, we assess the extent to which SIDM is required relative to CDM models that incorporate baryonic feedback and halo response.

Finally, in Section 5.5, we extend the comparison to the population level by examining how SIDM modifies key scaling relations in the galaxy–halo connection. In particular, we highlight that halo masses and concentrations inferred under SIDM can differ systematically from those derived assuming CDM, with important implications for interpreting galaxy–halo correlations.

5.1 Comparison with previous constraints

We note that the shape of the allowed region derived from our new model is consistent with previous kinematic constraints, which is based mainly on a much smaller subsample of the SPARC survey (Yang et al. 2024). However, a systematic offset exists between the two, as shown in the right panel of Fig. 5. We refrain from over-interpreting this difference, as the Yang et al. sample consists of only seven SPARC galaxies and two brightest cluster galaxies, which represents a biased subset of baryon-poor, spatially extended systems. These galaxies were selected partly because earlier versions of the isothermal Jeans model suffered from numerical robustness issues when applied to systems with compact and baryon-dominated inner regions. Under our updated selection criteria described in Section 3.1, we find that four of the seven SPARC galaxies do not qualify for inclusion, mainly because their rotation curves do not reach a clear plateau or maximum. For the remaining three SPARC galaxies common to both studies, we highlight their locations in the $\sigma_{\text{eff}}\text{--}V_{\text{max}}$ plane derived from our new model, as shown in the left panel of Fig. 5 – two of them indeed have best-fit cross sections on the lower end, with $\sigma_{\text{eff}} \lesssim 1 \text{ cm}^2 \text{ g}^{-1}$.

We also compare our constraints with previous constraints based on probes other than rotation curves. These include limits from central density estimates based on observations of stellar cores in ultra-faint dwarfs (Sánchez Almeida 2025) and Milky Way satellites (Correa 2021; Sloane et al. 2023), as well as constraints from strong lensing combined with stellar kinematics in groups and clusters (Sagunski et al. 2021; O’Donnell et al. 2025). Compared to our results, as shown in the left panel of Fig. 5, these studies exhibit good overall agreement and together strongly favor a cross section that decreases monotonically with velocity. In particular, the parameter space allowed by Sloane et al. (2023) shows remarkable overlap with our results, with our best-fit model lying well within their allowed region, as shown in the right panel of Fig. 5.

More intriguingly, the allowed region in our work is remarkably close to the cross-section values required to reproduce the supermassive black hole (SMBH) mass functions inferred for the Little Red

Dots in the early Universe (Jiang et al. 2026), which is characterized by $\sigma_0 \sim 20 - 30 \text{ cm}^2 \text{ g}^{-1}$ and $\omega \sim 80 - 120 \text{ km s}^{-1}$. In that cosmological framework, SMBHs form through the core-collapse of rare, early-forming, high-concentration SIDM halos. Taken together, these results suggest that the SIDM paradigm admits a region of parameter space that is simultaneously compatible with orthogonal constraints from nearby galaxy kinematics and from SMBH demographics at cosmic dawn.

5.2 Scatter in constraints on cross section

Our best-fit models result in substantial scatter observed in the $\sigma_{\text{eff}}\text{--}V_{\text{max}}$ plane. We find that this scatter largely originates from the limited constraining power on σ_{eff} from galaxies near the maximal-core stage of gravothermal evolution. We illustrate this point with the galaxy UGC07524, as shown in Fig. 6. For this system, we keep its M_{vir} and c fixed at the best-fit values and vary the product p by up to ± 0.5 dex. Within this wide range of p , the model rotation curves always remain roughly consistent with the data, because all these values correspond to a state near the maximal-core phase, during which the central density – and hence the overall density profile – is largely insensitive to changes in p . Hence, the cross section cannot be effectively constrained for *individual* systems near maximal core expansion. Approximately 40% of galaxies in our sample are near this evolutionary stage, leading to the large scatter in $\sigma_{\text{eff}}\text{--}V_{\text{max}}$ plane.

In addition, several aspects of both the data and the modeling remain uncertain or oversimplified. For example, while we allow different mass-to-light ratios for different galaxies – an improvement over earlier studies that assumed a constant value – we do not yet account for stellar-population gradients. Likewise, the modeling of baryonic distributions and adiabatic contraction can be refined with the aid of numerical simulations. We defer such improvements to future studies. We conclude that the large scatter in the $\sigma_{\text{eff}} - V_{\text{max}}$ distribution reflects a genuine limitation in constraining the SIDM cross section via rotation curve fitting, rather than evidence against the SIDM paradigm itself.

5.3 Comparison to CDM models with baryonic effects

We consider two CDM models that incorporate the structural response of halos to baryonic effects. First, we include the effect of adiabatic contraction on an NFW halo. This is directly analogous to the SIDM framework, where the target NFW halo contracts in response to a baryonic distribution described by a Hernquist profile, following the prescription of Gnedin et al. (2004). We refer to this as the *contracted NFW* model. Second, we adopt the empirical description of baryonic effects developed by Di Cintio et al. (2014), calibrated on hydrodynamical cosmological simulations. This model uses the $\alpha\beta\gamma$ parameterization of the density profile,

$$\rho(r) = \frac{\rho_s}{(r/r_s)^\gamma [1 + (r/r_s)^\alpha]^{(\beta-\gamma)/\alpha}}, \quad (22)$$

where the slopes are expressed as functions of the stellar-to-halo mass ratio, $X = \log(M_\star/M_{\text{vir}})$:

$$\alpha = 2.94 - \log[(10^{X+2.33})^{-1.08} + (10^{X+2.33})^{2.29}], \quad (23)$$

$$\beta = 4.23 + 1.34X + 0.26X^2, \quad (24)$$

$$\gamma = -0.06 + \log[(10^{X+2.56})^{-0.68} + (10^{X+2.56})]. \quad (25)$$

We refer to this as the DC14 model. For both CDM models, we adopt the same priors on halo mass and concentration, and use the same

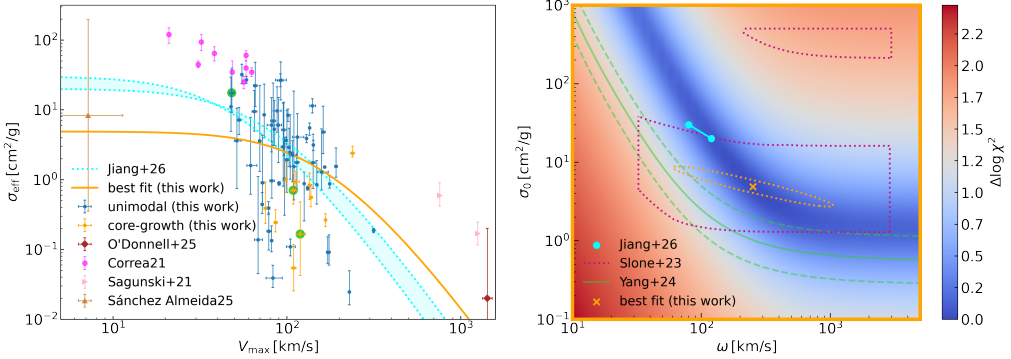


Figure 5. Comparison of constraints on the velocity-dependent SIDM cross section from this work with other studies across various scales. *Left:* The inferred effective cross section versus maximum circular velocity V_{\max} for the SPARC sample, taking the core-growth solution for bimodal cases. Blue (orange) points represent unimodal galaxies (the core-growth solution of bimodal galaxies) used in this study. Three of our galaxies are highlighted with green outlines, representing 1/3 of the sample analyzed by Yang et al. (2024), while their remaining SPARC galaxies fail to meet our selection criteria.). Points in other colors show constraints from previous studies using other probes: the stellar cores in ultra faint dwarfs (Sánchez Almeida 2025), Milky Way satellites (Correa 2021), strong lensing and stellar kinematics of groups and clusters (Sagunski et al. 2021; O'Donnell et al. 2025). *Right:* Joint constraints in the $\sigma_{\text{eff}} - \omega$ plane. The blue L-shaped region is from this work. Overlaid for comparison are the constraints from Yang et al. (2024) and Sloane et al. (2023). The orange cross marks the best-fit parameters adopting unimodal galaxies and the core-growth solutions of bimodal galaxies, with the surrounding ellipse approximating the 3σ posterior interval, the same as in Fig. 4. The Sloane et al. (2023) result (regions surrounded by purple dotted lines) has a significant overlap with our preferred region. Offset exists between our work and Yang et al. (2024), shown in green solid line with dashed lines indicating 1σ scatter. We refrain from over-interpreting this difference, as the Yang et al. sample is small and biased. The cyan point represents the cross sections required to reproduce the SMBH mass functions inferred for the Little Red Dots in the early Universe (Jiang et al. 2026), which lies closely to our allowed region.

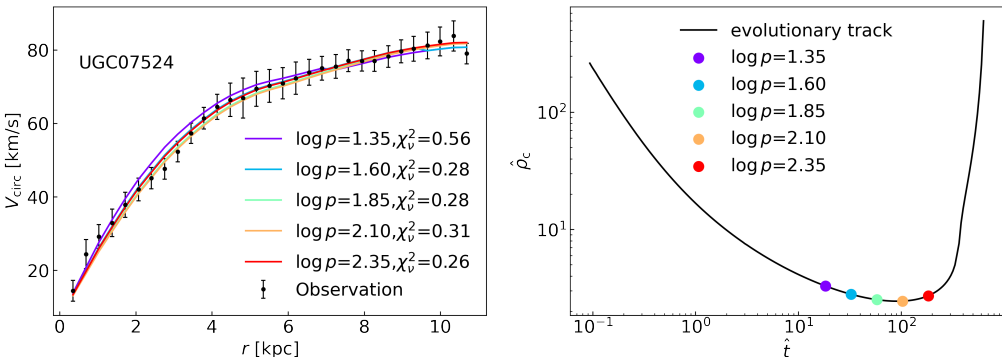


Figure 6. Illustration of limited constraining power on SIDM cross section for a halo near the maximal-core phase, using galaxy UGC07524 as an example. *Left:* observed rotation curve (black points) of UGC07524 with best-fit SIDM model (cyan line). Models with fixed halo mass and concentration but different product values p (colored lines) produce nearly identical rotation curves with similarly low χ^2_v , demonstrating the insensitivity of individual rotation curves to the cross section during this evolutionary stage. *Right:* gravothermal evolutionary track of the halo, in terms of normalized central density as a function of normalized time. The model rotation curves of different colors on the left correspond to points of the same colors on the right, which are all near the maximal-core stage.

MCMC sampling strategy as in the SIDM analysis to enable direct comparison.

We compare the two CDM baselines with our SIDM model using the reduced chi-square, χ^2_v , and the Bayesian Information Criterion (BIC, Schwarz 1978),

$$\text{BIC} = -2 \ln \mathcal{L} + k \ln n, \quad (26)$$

where k is the number of free parameters, n is the number of data points, and \mathcal{L} is the maximum likelihood. Models with smaller χ^2_v and BIC values are preferred. For SIDM double-solution systems, we adopt the better-fit solution.

As shown in Fig. 7, for about 80% of the sample, the SIDM model yield slightly better fits than the DC14 CDM model in terms of χ^2_v , and both outperform the contracted NFW model. The difficulty for the contracted NFW profile lies in producing central density cores, whereas DC14 (through baryonic feedback) and SIDM (through self-

scattering) can generate a spectrum of cusps and cores. The BIC comparison similarly disfavors contracted NFW relative to SIDM, and the SIDM and DC14 model have similar performance. This is because SIDM introduces additional free parameters (the cross-section parameters), while in DC14 the three profile slopes are tied directly to the stellar-to-halo mass ratio X , and thus do not increase the model's formal degrees of freedom.

5.4 Dark self-interaction or baryonic feedback?

One of the main effects of SIDM is the formation of density cores. However, cores can also be produced by baryonic feedback, particularly through gas outflows driven by supernovae (e.g., Freundlich et al. 2020). To rigorously disentangle these contributions, one would ideally employ an SIDM model that self-consistently includes baryonic feedback and allows each mechanism to be switched on or off

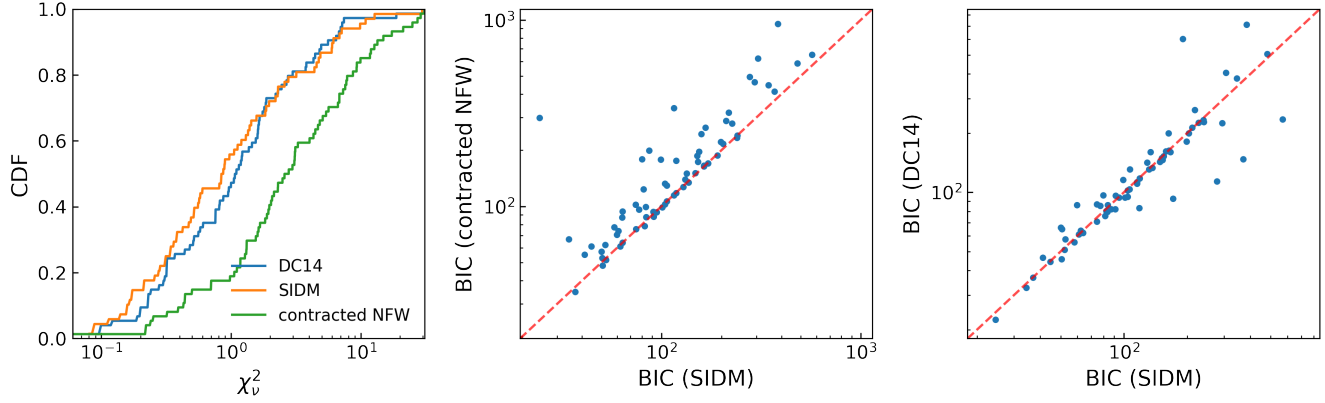


Figure 7. Cumulative distributions of reduced chi-square (χ^2_ν) (left) and Bayesian Information Criterion (BIC) comparisons (middle and right) for different models: the SIDM model developed in this study, the [Di Cintio et al. \(2014\)](#) CDM model with an empirical treatment of baryonic effects, and a simple CDM model with adiabatic contraction. The SIDM and DC14 models both provide significantly better fits than the adiabatic-contraction model, and have similar performance in terms of BIC.

in controlled experiments. While such an approach is beyond the scope of this work, we can still gain qualitative insight through the following analysis.

We ask whether the SIDM effect is degenerate with baryonic feedback. To do so, we take the effective cross section, σ_{eff} , as a proxy for the strength of SIDM, and the stellar-to-halo mass ratio M_\star/M_{vir} as a proxy for feedback strength. The reasoning is straightforward: baryonic core formation is expected to be strongest near $M_\star/M_{\text{vir}} \sim 0.01$ (e.g., [Di Cintio et al. 2014](#)). If σ_{eff} shows a local maximum in this regime, it would suggest that SIDM effects overlap or degenerate with baryonic feedback. Conversely, a lack of correlation would point to SIDM capturing distinct physical processes.

As shown in Fig. 8, we find no evidence for such a local maximum, and the correlation between σ_{eff} and M_\star/M_{vir} is essentially absent, with the Spearman correlation coefficient \mathcal{R} close to zero and its $p_{\mathcal{R}}$ value large. We therefore conclude that SIDM introduces a distinct channel for structural diversity in halos, separate from the effects of baryonic feedback.

5.5 SIDM impact on scaling relations

With a statistical sample, we are able to probe the stellar-to-halo mass relation (SHMR) in the SIDM framework and compare it directly with CDM results. For simplicity, we adopt the core-growth solution for galaxies with bimodal posteriors. The left panel of Fig. 9 shows the SHMR for the 68 SPARC galaxies in our analysis. For reference, we include the abundance-matching relations of [Moster et al. \(2013\)](#) and [Garrison-Kimmel et al. \(2017\)](#), adopting the growing-scatter model for field galaxies, both based on Λ CDM cosmological simulations. These two CDM relations differ by nearly 0.5 dex in halo mass at fixed stellar mass, underscoring the substantial uncertainty in the dwarf-galaxy regime of the SHMR even within Λ CDM. We identify six galaxies that exhibit the highest total star-formation efficiency $f_\star \equiv M_\star/(f_b M_{\text{vir}})$ in our SIDM fits, where $f_b \equiv 0.188$ is the cosmological baryon fraction. In the left panel of Fig. 9, these systems (red points) reside in halos that are ~ 0.5 dex less massive than predicted by the CDM reference relations at the same stellar mass.

The middle and right panels of Fig. 9 recast the SHMR in the form of f_\star as a function of stellar mass, and compare the SIDM

and DC14 results side by side. Both fits are broadly consistent with the [Moster et al. \(2013\)](#) for bright dwarfs ($M_\star \approx 10^7 - 10^9 M_\odot$). However, the same six high- f_\star galaxies show values close to unity in the SIDM case, which is a significant deviation from both the [Moster et al. \(2013\)](#) and [Garrison-Kimmel et al. \(2017\)](#) relations. This discrepancy is not seen in the DC14 fits, where galaxies at the high-mass end remain consistent with the CDM SHMR.

We note that a similar departure from the SHMR for disc galaxies has been reported in earlier CDM-based studies ([Posti et al. 2019](#)). Notably, the two galaxies with $f_\star > 1$ identified in [Posti et al. \(2019\)](#), NGC5371 and NGC0801, correspond to the two systems with the highest f_\star in our present analysis. Hence the deviation does not uniquely distinguish between dark-matter scenarios, but indicates that the tension persists even when a new dark-matter species is assumed. We suspect that an overestimated mass-to-light ratio leads to the departure observed in both [Posti et al. \(2019\)](#) and our work. To examine the origin of the difference between SIDM and DC14 fits, we also mark the same six galaxies with red circles in the right panel of Fig. 9. Among them, three have unreliable mass constraints $V_{\text{vir}}/V_{\text{max}} \gtrsim 1$ and also show the lowest f_\star values within the group. The remaining three galaxies have virial masses roughly 0.5 dex larger in the DC14 fit than in the SIDM fit.

In addition, we examine the halo concentration - halo mass relation, again, adopting the core-growth solution in bimodal cases for SIDM fits. The results are shown in Fig. 10. The reference line indicates the widely used empirical concentration-mass relation of [Dutton & Macciò \(2014\)](#) (DM14). Since this relation is included as a prior for both the SIDM and DC14 fits, it is not surprising that the resulting c - M_{vir} relations broadly follow the input trend. However, a notable difference emerges: the SIDM mass models produce a systematically lower concentration than the DM14. To quantify this offset, we assume $\log c$ obeys Gaussian distribution, with a constant standard deviation σ and the median described by a linear relation, $\log c = k \log M_{\text{vir}} + b$, where σ , k , and b are free parameters. We fit this simple relation to the results of both CDM and SIDM models. As clearly visible in Fig. 10, the median SIDM relation is below DM14, while the slope is similar. The fit to DC14 results shows a steeper slope and a higher normalization. Both SIDM and DC14 re-

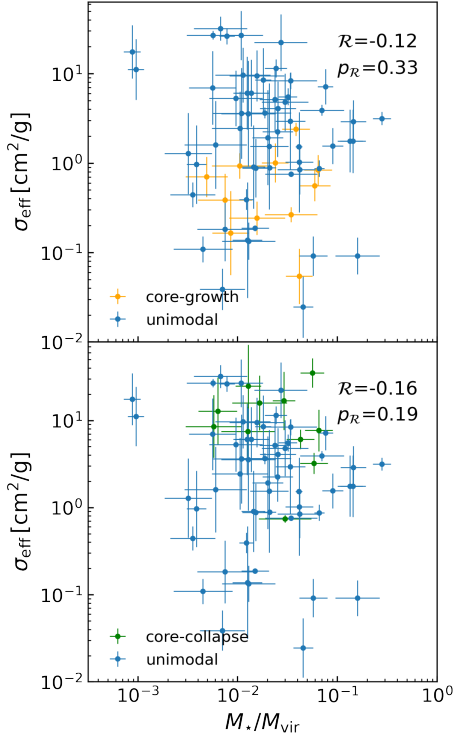


Figure 8. Correlation between the SIDM effect, quantified by the effective cross section σ_{eff} , and baryonic effects, proxied by the stellar-to-halo mass ratio M_*/M_{vir} . In the *upper* and *lower* panels, the orange and green symbols represent the core-growth and core-collapse solutions, respectively, for galaxies with bimodal posteriors. Galaxies with unimodal posteriors are shown in blue. The Spearman correlation coefficients \mathcal{R} and their associated $p_{\mathcal{R}}$ values are reported in each panel. Overall, the correlations are weak to absent. These results suggest that SIDM introduces a distinct source of structural diversity in halos, largely independent of baryonic feedback effects.

sults show slightly larger scatters, $\sigma_{\text{SIDM}} = 0.159$ and $\sigma_{\text{DC14}} = 0.176$ respectively, compared to DM14 ($\sigma_{\text{DM14}} = 0.11$).

6 CONCLUSION

In this study, we have improved the semi-analytical isothermal Jeans model for computing self-interacting dark matter (SIDM) halo profiles, and applied it to constrain the self-scattering cross section using rotation curves from the SPARC survey. Our advances include incorporating velocity-dependent cross sections through an effective cross section formalism (Yang & Yu 2022), improving numerical stability over the previous implementation (Jiang et al. 2023), and adopting an empirical treatment of gravothermal core collapse (Yang et al. 2024). These improvements allow us to model a larger and more diverse galaxy sample, including systems with cuspy or baryon-dominated centers that were often excluded in earlier studies.

Analyzing 68 SPARC galaxies, we find that about 1/6 exhibit bimodal posteriors in the parameter space spanned by halo mass, concentration, and effective cross section (or rather, the product of effective cross section and halo age). This bimodality arises because core-growth and core-collapse halos of similar mass and concentration can yield similar density profiles. We interpret this as tentative evidence for the presence of core-collapsing halos in the SIDM framework. Among unimodal systems, about 50% are consistent

with being at the maximal-core stage, while the rest are best fit in the core-expanding phases.

From these models we derive constraints on the velocity-dependent cross-section parameters, σ_0 and ω . Two scenarios were considered depending on how bimodal systems are treated. The effective cross section σ_{eff} anti-correlates strongly with the maximum circular velocity V_{max} , yielding a well-defined L-shaped degeneracy in the (σ_0, ω) plane, and the shape is not sensitive to the choice of solutions for bimodal cases. Both nearly constant cross sections ($\sigma_0 \sim 2 \text{ cm}^2/\text{g}$, $\omega \gtrsim 500 \text{ km/s}$) and strongly velocity-dependent ones ($\sigma_0 \sim 100 \text{ cm}^2/\text{g}$, $\omega \sim 60 \text{ km/s}$) are comparably viable. Fitting the $(V_{\text{max}}, \sigma_{\text{eff}})$ data gives representative best-fit parameters of $(\sigma_0, \omega) = (4.9 \text{ cm}^2/\text{g}, 250 \text{ km/s})$ or $(6 \text{ cm}^2/\text{g}, 220 \text{ km/s})$, depending on the assumed evolutionary branch for the bimodal galaxies.

We find that the parameter space favored by our model is broadly consistent with previous constraints from nearby galaxies, while also encompassing values that independently explain the supermassive black hole mass functions inferred for the Little Red Dots at high redshift (Jiang et al. 2026). Taken together, these results highlight a region of SIDM parameter space that simultaneously satisfies orthogonal constraints from local galaxy dynamics and black-hole demographics in the early Universe.

We also compare our SIDM model against two cold dark matter (CDM) models that incorporate baryonic effects: a contracted NFW profile and the empirical Di Cintio et al. (2014, DC14) model. SIDM and DC14 outperform the simple contraction model, and have similar performance in BIC. Given that CDM simulations still disagree on the strength of core formation driven by baryonic feedback, the fact that SIDM naturally generates both cores and cusps without invoking fine-tuned baryonic physics remains a key advantage. Moreover, the effective cross sections from our fits show marginal correlations with the stellar fraction – a proxy for feedback strength, suggesting that SIDM accounts for structural diversity in a way distinct from baryonic feedback.

Finally, we explore implications for galaxy–halo scaling relations. The stellar-to-halo mass relation (SHMR) from SIDM fits shows that the total star-formation efficiency $M_*/(f_b M_{\text{vir}})$ of some galaxies exceeds the prediction of CDM SHMR and, in a couple of cases, close to unity. This is not unique to the SIDM mass models: previous CDM-based mass models by Posti et al. (2019) reveal similar cases. We conclude that SIDM does not significantly vary the SHMR. In addition, we find that the SIDM concentration–mass relation systematically falls below the CDM relation (Dutton & Macciò 2014)

In summary, our analysis demonstrates that SIDM can successfully reproduce the diversity of galaxy rotation curves, but also highlights key degeneracies and the broad scatter in inferred cross sections. The joint constraints consistently favor velocity-dependent interactions, with the characteristic L-shaped degeneracy in the (σ_0, ω) plane. These results underscore both the potential and the limitations of current SIDM modeling: the framework captures essential features of galactic kinematics, yet no single cross-section model fits the entire galaxy sample. Breaking these degeneracies using nearby kinematics will require improved theoretical treatments and new kinematic data, especially for ultra-faint dwarfs at $V_{\text{max}} \lesssim 30 \text{ km/s}$.

ACKNOWLEDGEMENTS

We thank Haibo Yu, Daneng Yang, and Luis Ho for insightful comments and suggestions. This work is supported by the China Manned Space Program with Grant No. CMS-CSST-2025-A03. FJ acknowledges support from the National Natural Science Foundation of China

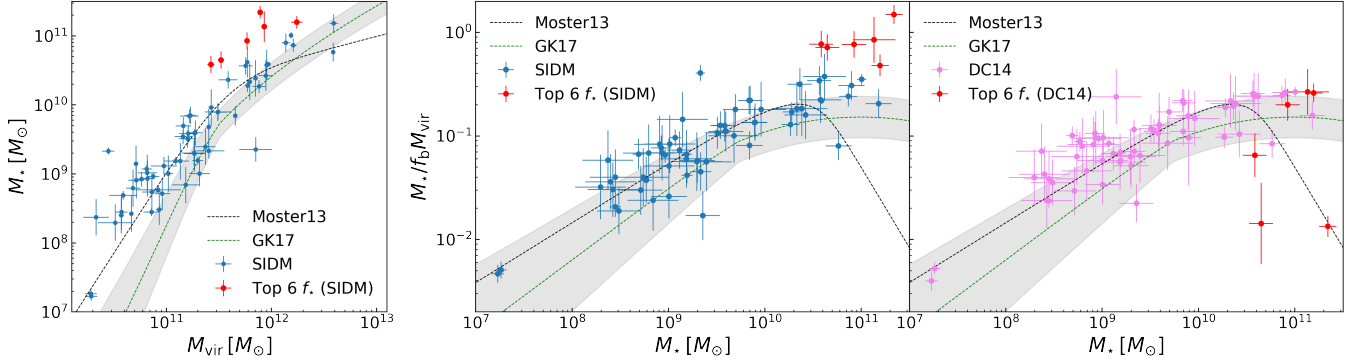


Figure 9. Stellar-mass-total-mass relations (SHMRs) shown as M_* versus M_{vir} (left), and as the star-formation-efficiency ratio $f_* \equiv M_*/(f_b M_{\text{vir}})$ versus M_* (middle and right). For simplicity, we focus on the core-growth solutions for galaxies with bimodal posteriors, together with unimodal systems. The right panel compares our SIDM results to those obtained under the CDM framework using the Di Cintio et al. (2014) model. Relative to the reference relations from Moster et al. (2013) (black line) and Garrison-Kimmel et al. (2017) (green line, with the shaded band marking the 1σ scatter), SIDM fits systematically yield lower halo masses and correspondingly higher f_* at the high-stellar-mass end, whereas DC14 results remain broadly consistent with the CDM expectations. Red circles in all panels mark the six galaxies with the highest f_* in our SIDM fits. We note that a similar discrepancy at high-stellar-mass end has been reported in earlier CDM-based studies of disc galaxies (Posti et al. 2019), which suggests that the tension is not resolved by introducing SIDM. Our results thus reaffirm the existence of high- f_* outliers even within an SIDM scenario.

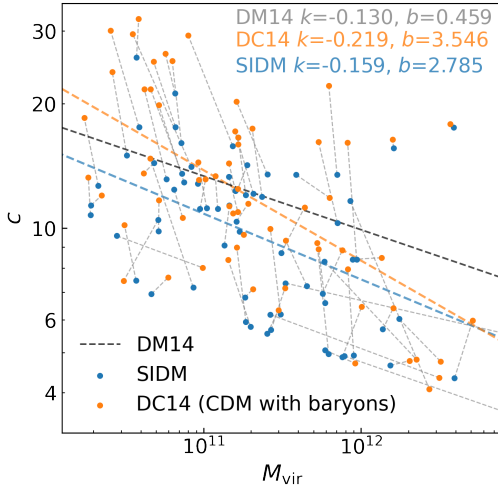


Figure 10. Halo concentration-mass relation derived from our SIDM mass models and the Di Cintio et al. (2014) CDM models. For galaxies with bimodal SIDM posteriors, we adopt the core-growth solution. CDM and SIDM results for the same galaxy are connected by gray dashed lines. The black dashed line marks the Dutton & Macciò (2014) concentration-mass relation, and the blue and orange dashed lines respectively represent the best-fit concentration-mass relations derived from the SIDM and DC14 fits, with their slopes and intercepts provided in the panel. We find that SIDM yields systematically lower concentrations than the DM14 reference relation, albeit with a similar slope. In contrast, the DC14 fits result in both a steeper slope and a higher normalization of the relation.

(NSFC, Grant No. 12473007). ZJ acknowledges support from the Beijing Natural Science Foundation (Grant No. QY23018). RL acknowledges the support of NSFC (Grant No. 11988101) and CAS Project for Young Scientists in Basic Research (No. YSBR-062). LZ acknowledges the support from CAS Project for Young Scientists in Basic Research, Grant No. YSBR-062 and National Key R&D Program of China No. 2025YFF0511000.

DATA AVAILABILITY

The improved isothermal Jeans model developed in this work is publicly available at: https://github.com/ZixiangJia/SIDM_Jeans_model, and the version in development is available upon request to the corresponding author. The data used in the analysis is publicly available at the SPARC survey website: <https://astroweb.cwru.edu/SPARC/>. The fitting results can be found at https://github.com/ZixiangJia/Jia26_fitting_results.

APPENDIX A: IMPROVEMENT ON THE ISOTHERMAL JEANS MODEL

In this appendix, we detail the improvements on the Jeans model. To extend the Jeans model into the core-collapse regime, following Yang et al. (2024), we approximate the density profile of a core-collapsed halo with a given product p using the high-density solution evaluated at $p' = 2p_{\text{merge}} - p$. To implement this, we develop an efficient algorithm that accurately determines the merge point $p_{\text{merge}} = \sigma_{\text{eff}} t_{\text{merge}}$. We further refine the stitching procedure by introducing a criterion to exclude non-physical outcomes and performing multiple searches across partitioned intervals in parameter space. This enhancement allows robust identification of both the low-density and high-density solution branches. Together, these improvements support fast and reliable computation of the Jeans model across all stages of halo evolution.

A1 Calculation of the merge point of the halo

We employ a bisection method to precisely determine the merge point p_{merge} of a halo. This approach is based on a characteristic feature of the Jeans model: assuming Eq. (1), when $p > p_{\text{merge}}$, the model yields only physically invalid solutions, whereas for $p < p_{\text{merge}}$, at least one valid solution can be obtained through sufficient searching. To quantify this behavior, we propose that the objective quantity

$$\delta^2 = \left[\frac{\rho_{\text{iso}}(r_1) - \rho_{\text{cdm}}(r_1)}{\rho_{\text{cdm}}(r_1)} \right]^2 + \left[\frac{M_{\text{iso}}(r_1) - M_{\text{cdm}}(r_1)}{M_{\text{cdm}}(r_1)} \right]^2, \quad (\text{A1})$$

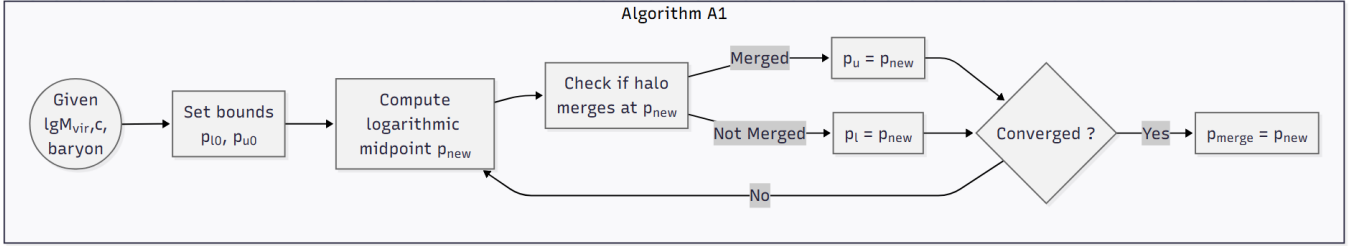


Figure A1. Flowcharts of algorithm A1 (details in Appendix A1), which implements a bisection method for determining the halo merge point p_{merge} . Starting from initial bounds p_{10} (pre-merger) and p_{00} (post-merger), the algorithm iteratively narrows the interval containing p_{merge} by testing whether the isothermal Jeans solutions have merged at the logarithmic midpoint p_{new} . This step is essential for subsequently approximating the density profile of a core-collapsed halo via the high-density-solution-mirroring technique.

which quantifies the deviation from the boundary conditions required by the Poisson equation, serves as an effective indicator of invalid solutions. Empirically, we find that $\delta^2 < 10^{-5}$ provides a reliable threshold for selecting physically meaningful solutions. Leveraging this clear transition and the aforementioned characteristic behavior of the model, we construct a bisection algorithm to precisely locate p_{merge} , with the flowchart of the algorithm shown in Fig. A1.

The algorithm proceeds as follows. We first select an initial lower bound p_{10} (in the pre-merger regime) and an upper bound p_{00} (in the post-merger regime). The logarithmic midpoint is then calculated as $\log p_{\text{new}} = (\log p_{10} + \log p_{00})/2$. To exclude the cases where a single search fails to find a valid solution when $p < p_{\text{merge}}$, we perform four independent searches with different initial guesses and evaluate their δ^2 . A halo is considered to have merged ($p > p_{\text{merge}}$) only if all four searches return $\delta^2 > 10^{-5}$. After assessing the halo state at p_{new} , if the halo has merged, we update the upper bound to $p_{01} = p_{\text{new}}$ while retaining the lower bound $p_{11} = p_{10}$. If it has not merged, the lower bound is updated to $p_{11} = p_{\text{new}}$ and the upper bound remains $p_{01} = p_{00}$. This process iterates until the bounds satisfy a specified convergence criterion, at which point the final p_{new} is returned as the merge point. The entire bisection scheme enables the precise determination of a halo’s merge point within seconds.

A2 Robustly identifying the solution

The stitching process occasionally converges to saddle points or parameter space boundaries when $p < p_{\text{merge}}$, leading to an invalid solution. To robustly identify physically valid solutions across all evolutionary stages of the halo, we partition the search intervals and perform multiple searches from different initial positions. This approach substantially improves the robustness of the solution identification and ensures reliable outputs.

For halos at different evolutionary stages, we employ distinct search strategies. We define the normalized halo age as $\hat{t} \equiv 8\sqrt{G\rho_s\rho_s r_s \sigma_{\text{eff}} t_{\text{age}}} \propto p$, and let \hat{t}_0 denote the point at which the normalized central density $\hat{\rho}_c \equiv \rho_c/\rho_s$ equals that at the merge point $\hat{\rho}_{\text{merge}} \equiv \hat{\rho}_c(\hat{t} = \hat{t}_{\text{merge}})$, where \hat{t}_{merge} is the normalized age corresponding to p_{merge} . The evolution of an SIDM halo is divided into three stages based on \hat{t}_0 and \hat{t}_{merge} , as illustrated in Fig. A2.

When $\hat{t} \leq \hat{t}_0$ (region A in Fig. A2), the corresponding mirrored solution with $\hat{t}' = 2\hat{t}_{\text{merge}} - \hat{t}$ would lie deep in the collapsed regime, beyond the predictive range of the Jeans model. Hence we assume that a high-density branch does not exist in this stage. In this case, we require the lower limit of the search interval of $\rho_{\text{dm}0}$ to be ρ_{merge} , the central density at \hat{t}_{merge} .

When $\hat{t}_0 \leq \hat{t} < \hat{t}_{\text{merge}}$ (region C), the model is expected to yield

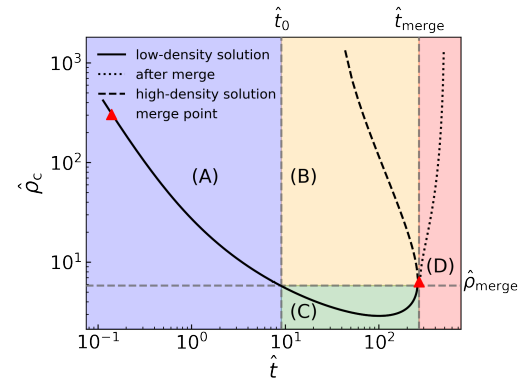


Figure A2. Gravothermal evolutionary stages of an SIDM halo, divided based on the normalized central density $\hat{\rho}$ as a function of the normalized age \hat{t} . Two dashed vertical lines denote the transition boundaries \hat{t}_0 and \hat{t}_{merge} , separating the evolution into the three distinct regimes employed in the Jeans model. Here, \hat{t}_0 corresponds to the point where the normalized central density $\hat{\rho}_c$ equals its value at the merge point $\hat{\rho}_{\text{merge}} \equiv \hat{\rho}_c(\hat{t} = \hat{t}_{\text{merge}})$, with \hat{t}_{merge} representing the normalized age at p_{merge} .

the low-density solution. Here we impose ρ_{merge} as the upper bound of the $\rho_{\text{dm}0}$ search interval.

When $\hat{t} \geq \hat{t}_{\text{merge}}$ (region D), we approximate the density profile using the high-density solution evaluated at the mirrored age $\hat{t}' = 2\hat{t}_{\text{merge}} - \hat{t}$, which lies in region B. For this regime, the lower bound of the $\rho_{\text{dm}0}$ search is again set to ρ_{merge} .

For a given halo, we first check whether its product p exceeds p_{merge} . If so, the solution of the Jeans model lies in region D; in this case, we approximate it using the high-density solution in region B. Otherwise, we examine whether the solution resides in region C by constraining the upper bound of the search interval for $\rho_{\text{dm}0}$ to ρ_{merge} . If all search attempts return physically invalid outcomes, we conclude that the solution belongs to region A and execute the corresponding search strategy accordingly.

In all regimes, search for $(\rho_{\text{dm}0}, v_0)$ is performed with up to 20 independent attempts from different initial guesses. Solutions that yield $\delta^2 > 10^{-5}$ are rejected as physically invalid. This multi-search strategy, combined with the stage-dependent bounds, ensures robust identification of the appropriate solution branch across the entire evolution of an SIDM halo.

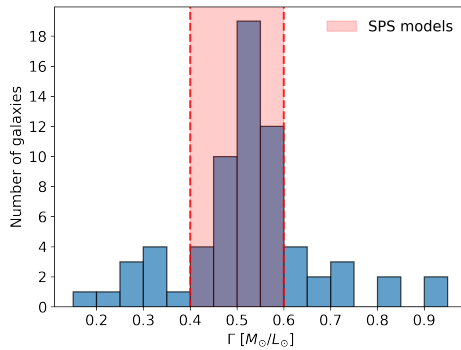


Figure B1. Distribution of mass-to-light ratio Γ at $3.6 \mu\text{m}$ for the 68 galaxies in our study. The vertical shaded band marks the range $\Gamma = 0.4 – 0.6 M_\odot/L_\odot$, as predicted by stellar population synthesis (SPS) models, depending on the model and initial mass function (Lelli et al. 2016). The histogram shows that the majority of galaxies lie within this theoretical range, confirming that our adopted mass-to-light ratio values are generally consistent with SPS expectations.

APPENDIX B: MASS-TO-LIGHT RATIO

In this appendix, we demonstrate that the mass-to-light ratio derived in this study are generally consistent with the predictions of stellar population synthesis (SPS) models. According to Lelli et al. (2016), SPS models yield an average mass-to-light ratio at $3.6 \mu\text{m}$ in the range of $0.4–0.6 M_\odot/L_\odot$, depending on the specific model and initial mass function (IMF). In Fig. B1, we present the distribution of the mass-to-light ratios for the 68 galaxies in our study. As shown, the majority of galaxies fall within the range predicted by SPS models, which shows general agreement with theoretical expectations.

REFERENCES

Adhikari S., Banerjee A., Jain B., Hyeon-Shin T., Zhong Y.-M., 2024, arXiv e-prints, p. arXiv:2401.05788

Balberg S., Shapiro S. L., Inagaki S., 2002, *ApJ*, **568**, 475

Bullock J. S., Boylan-Kolchin M., 2017, *ARA&A*, **55**, 343

Correa C. A., 2021, *MNRAS*, **503**, 920

Di Cintio A., Brook C. B., Dutton A. A., Macciò A. V., Stinson G. S., Knebe A., 2014, *MNRAS*, **441**, 2986

Dutton A. A., Macciò A. V., 2014, *MNRAS*, **441**, 3359

Einasto J., 1965, Trudy Astrofizicheskogo Instituta Alma-Ata, **5**, 87

Elbert O. D., Bullock J. S., Garrison-Kimmel S., Rocha M., Oñorbe J., Peter A. H. G., 2015, *MNRAS*, **453**, 29

Essig R., McDermott S. D., Yu H.-B., Zhong Y.-M., 2019, *Phys. Rev. Lett.*, **123**, 121102

Foreman-Mackey D., Hogg D. W., Lang D., Goodman J., 2013, *PASP*, **125**, 306

Freundlich J., et al., 2020, *MNRAS*, **499**, 2912

Garrison-Kimmel S., Bullock J. S., Boylan-Kolchin M., Bardwell E., 2017, *MNRAS*, **464**, 3108

Gilman D., Bovy J., Treu T., Nierenberg A., Birrer S., Benson A., Sameie O., 2021, *MNRAS*, **507**, 2432

Gnedin O. Y., Kravtsov A. V., Klypin A. A., Nagai D., 2004, *ApJ*, **616**, 16

Jiang F., Dekel A., Freundlich J., van den Bosch F. C., Green S. B., Hopkins P. F., Benson A., Du X., 2021, *MNRAS*, **502**, 621

Jiang F., et al., 2023, *MNRAS*, **521**, 4630

Jiang F., Jia Z., Zheng H., Ho L. C., Inayoshi K., Shen X., Vogelsberger M., Feng W.-X., 2026, *ApJ*, **996**, L19

Kamada A., Kaplinghat M., Pace A. B., Yu H.-B., 2017, *Phys. Rev. Lett.*, **119**, 111102

Kaplinghat M., Keeley R. E., Linden T., Yu H.-B., 2014, *Phys. Rev. Lett.*, **113**, 021302

Kaplinghat M., Tulin S., Yu H.-B., 2016, *Phys. Rev. Lett.*, **116**, 041302

Komatsu E., et al., 2011, *ApJS*, **192**, 18

Kong D., Yu H.-B., 2025, *Physics of the Dark Universe*, **48**, 101939

Lacey C., Cole S., 1993, *MNRAS*, **262**, 627

Lelli F., McGaugh S. S., Schombert J. M., 2016, *AJ*, **152**, 157

Li P., Lelli F., McGaugh S., Schombert J., 2020, *ApJS*, **247**, 31

Li S., et al., 2025, arXiv e-prints, p. arXiv:2504.11800

Moster B. P., Naab T., White S. D. M., 2013, *MNRAS*, **428**, 3121

Nadler E. O., Yang D., Yu H.-B., 2023, *ApJ*, **958**, L39

Navarro J. F., Frenk C. S., White S. D. M., 1997, *ApJ*, **490**, 493

Nishikawa H., Boddy K. K., Kaplinghat M., 2020, *Phys. Rev. D*, **101**, 063009

O'Donnell J. H., Jeltema T. E., Roberts M. G., Nightingale J., Flowers A., Aldas D., 2025, arXiv e-prints, p. arXiv:2508.20179

Pedregosa F., et al., 2011, Journal of Machine Learning Research, **12**, 2825

Pollack J., Spergel D. N., Steinhardt P. J., 2015, *ApJ*, **804**, 131

Posti L., Fraternali F., Marasco A., 2019, *A&A*, **626**, A56

Read J. I., Agertz O., Collins M. L. M., 2016, *Monthly Notices of the Royal Astronomical Society*, **459**, 2573

Ren T., Kwa A., Kaplinghat M., Yu H.-B., 2019, *Physical Review X*, **9**, 031020

Roberts M. G., Kaplinghat M., Valli M., Yu H.-B., 2024, arXiv e-prints, p. arXiv:2407.15005

Robertson A., Massey R., Eke V., Schaye J., Theuns T., 2020, *Monthly Notices of the Royal Astronomical Society*, **501**, 4610

Robles V. H., et al., 2017, *MNRAS*, **472**, 2945

Rocha M., Peter A. H. G., Bullock J. S., Kaplinghat M., Garrison-Kimmel S., Oñorbe J., Moustakas L. A., 2013, *MNRAS*, **430**, 81

Sagunski L., Gad-Nasr S., Colquhoun B., Robertson A., Tulin S., 2021, *J. Cosmology Astropart. Phys.*, **2021**, 024

Sales L. V., Wetzel A., Fattah A., 2022, *Nature Astronomy*, **6**, 897

Sánchez Almeida J., 2025, *A&A*, **704**, A210

Schwarz G., 1978, *Annals of Statistics*, **6**, 461

Slone O., Jiang F., Lisanti M., Kaplinghat M., 2023, *Phys. Rev. D*, **107**, 043014

Tulin S., Yu H.-B., 2018, *Phys. Rep.*, **730**, 1

Weinberg D. H., Bullock J. S., Governato F., Kuzio de Naray R., Peter A. H. G., 2015, *Proceedings of the National Academy of Science*, **112**, 12249

Yang D., Yu H.-B., 2022, *J. Cosmology Astropart. Phys.*, **2022**, 077

Yang D., Nadler E. O., Yu H.-B., 2023, *ApJ*, **949**, 67

Yang S., et al., 2024, *MNRAS*, **533**, 4007

This paper has been typeset from a *TeX/LaTeX* file prepared by the author.